

Active region chromospheric magnetic fields

Observational inference versus magnetohydrostatic modelling

G. J. M. Vissers¹, S. Danilovic¹, X. Zhu^{2,3}, J. Leenaarts¹, C. J. Díaz Baso¹, J. M. da Silva Santos¹, J. de la Cruz Rodríguez¹, and T. Wiegmann³

¹ Institute for Solar Physics, Department of Astronomy, Stockholm University, AlbaNova University Centre, 106 91 Stockholm, Sweden

² CAS Key Laboratory of Solar Activity, National Astronomical Observatories, Chinese Academy of Sciences, Beijing, China

³ Max Planck Institute for Solar System Research, Justus-von-Liebig-Weg 3, 37077 Göttingen, Germany

ABSTRACT

Context. A proper estimate of the chromospheric magnetic fields is believed to improve modelling of both active region and coronal mass ejection evolution. However, since the chromospheric field is not regularly obtained for sufficiently large fields-of-view, estimates thereof are commonly obtained through data-driven models or field extrapolations, based on photospheric boundary conditions alone and involving pre-processing that may reduce details and dynamic range in the magnetograms.

Aims. We investigate the similarity between the chromospheric magnetic field that is directly inferred from observations and the field obtained from a magnetohydrostatic (MHS) extrapolation based on a high-resolution photospheric magnetogram.

Methods. Based on Swedish 1-m Solar Telescope Fe I 6173 Å and Ca II 8542 Å observations of NOAA active region 12723, we employed the spatially-regularised weak-field approximation (WFA) to derive the vector magnetic field in the chromosphere from Ca II, as well as non-LTE inversions of Fe I and Ca II to infer a model atmosphere for selected regions. Milne-Eddington inversions of Fe I serve as photospheric boundary conditions for the MHS model that delivers the three-dimensional field, gas pressure and density self-consistently.

Results. For the line-of-sight component, the MHS chromospheric field generally agrees with the non-LTE inversions and WFA, but tends to be weaker than those when larger in magnitude than 300 G. The observationally inferred transverse component is systematically stronger, up to an order of magnitude in magnetically weaker regions, yet the qualitative distribution with height is similar to the MHS results. For either field component the MHS chromospheric field lacks the fine structure derived from the inversions. Furthermore, the MHS model does not recover the magnetic imprint from a set of high fibrils connecting the main polarities.

Conclusions. The MHS extrapolation and WFA provide a qualitatively similar chromospheric field, where the azimuth of the former is better aligned with Ca II 8542 Å fibrils than that of the WFA, especially outside strong-field concentrations. The amount of structure as well as the transverse field strengths are, however, underestimated by the MHS extrapolation. This underscores the importance of considering a chromospheric magnetic field constraint in data-driven modelling of active regions, particularly in the context of space weather predictions.

Key words. Sun: activity – Sun: chromosphere – Sun: photosphere – Sun: magnetic topology – Radiative transfer

1. Introduction

Our monitoring capabilities of solar activity drastically improved with the 24/7 coverage from the photosphere to the corona that the *Solar Dynamics Observatory* (SDO; Pesnell et al. 2012) and its two instruments, the *Atmospheric Imaging Assembly* (AIA; Lemen et al. 2012), and *Helioseismic and Magnetic Imager* (HMI; Scherrer et al. 2012, Schou et al. 2012) afford since early 2010. SDO/HMI provides full-disk photospheric vector-magnetograms that have been used as basis for field extrapolations and bottom boundary conditions in data-driven modelling of, for instance, flare-productive active regions (e.g. Jin et al. 2016, Price et al. 2020). Similar observations are not currently obtained on a routine basis for the chromospheric magnetic field¹, while several studies indicate that including the chromospheric field vector is beneficial both for data-driven modelling

and recovering chromospheric and coronal magnetic field structures in extrapolations (e.g. De Rosa et al. 2009, Fleishman et al. 2019, Toriumi et al. 2020). A chromospheric field constraint on erupting flux ropes could also aid in modelling and forecasting coronal mass ejection (CME) evolution, thereby likely improving the predictions for the geo-effectiveness of CMEs (Kilpua et al. 2019).

In the absence of chromospheric constraints, data-driven modelling relies on magnetic (and electric) field boundary conditions from the photosphere alone (but see Metcalf et al. 2008, Wiegmann et al. 2008). Depending on the modelling approach, the HMI magnetograms are passed through several pre-processing steps that serve to e.g. avoid flux-imbalance and nudge the bottom boundary to a force-free state or ensure numerical stability, but these may also impact the modelled field configuration in the higher atmosphere. For instance, Vissers et al. (2021), analysing an X2.2 flare, report discrepancies that can in part be attributed to the pre-processing that smoothes and modifies the photospheric field, but they also point out the importance of higher resolution in the modelling to uncover de-

¹ The SOLIS (Synoptic Optical Long-term Investigations of the Sun; Keller et al. 2003) Vector Spectromagnetograph did provide near-daily full-disk line-of-sight chromospheric magnetograms using Ca II 8542 Å until late October 2017, but has not been operational since.

tails in the chromospheric atmospheric field configuration. Both likely affect the photospheric and chromospheric field estimates and may thus have implications for the space-weather modelling that builds on such data-driven models. The magnetohydrostatic (MHS) model (Zhu & Wiegmann 2018, 2019, Zhu et al. 2020) that we consider here includes part of the aforementioned pre-processing, but uses the original photospheric magnetogram as bottom boundary condition while iteratively reaching a solution, which could yield a better estimate of the chromospheric field configuration.

With current instrumentation the field-of-view (FOV) for high-resolution chromospheric observations is often constrained to some $50''$ – $70''$ on the side, meaning that larger active regions (or flux ropes for that matter) cannot typically be contained entirely within a single pointing, thereby limiting the benefits from incorporating such observations as boundary conditions for modelling larger-scale structures. A solution to this is to canvas extended regions by mosaicking (e.g. Reardon & Cauzzi 2012, Hammerschlag et al. 2013), but such observations have not been common practice at the Swedish 1-m Solar Telescope (SST; Scharmer et al. 2003). Indeed, only one such study exists (Sculion et al. 2014), presenting a 9×6 mosaic that covers an active region with a FOV of $280''\times 180''$ in $H\alpha$ imaging spectroscopy. However, recent improvements in the SST pointing control software have now rendered mosaicking a relatively simple task.

Here we analyse a flux-balanced mosaic of NOAA active region (AR) 12723 and compare its chromospheric magnetic field as inferred from the observations with that from a MHS model based on a high-resolution photospheric vector magnetogram. A spatially-regularised weak-field approximation (WFA) delivers the full-FOV chromospheric magnetic field, while we use Milne-Eddington (ME) inversions to obtain the photospheric field vector, which also serves as boundary condition for the MHS extrapolation model. Furthermore, we perform non-LTE inversions of selected regions-of-interest (ROIs) to allow a depth-stratified comparison with the MHS model.

The remainder of this publication is structured as follows. Section 2 introduces the observations, mosaic construction and post-processing to prepare the data for inversions. Section 3 describes the ME, WFA and non-LTE inversion techniques used to infer the photospheric and chromospheric magnetic field vectors, as well as the MHS model setup. We present our results in Section 4, considering the field vector both for several regions of interest and on larger, active region scales. Finally, we discuss our findings in Section 5 and present our conclusions in Section 6.

2. Observations and reduction

On 30 September 2018 we observed NOAA AR 12723 with the the CRisp Imaging SpectroPolarimeter (CRISP; Scharmer et al. 2008) and CHROMIS (Scharmer 2017) at the SST. These observations consist of two rounds of four overlapping pointings in a 2×2 pattern for a context mosaic, followed by a regular, single-pointing time series. For this study, we focus only on the context data and selected the set of pointings with the highest image contrast to construct the mosaic that we analyse here.

The mosaic has a mean observing time of 09:24:03 UT, is centred at $(X, Y) = (95'', -270'')$, corresponding to $\mu = 0.95$, and covers about $110''\times 110''$ at 0.058 pix^{-1} . Figure 1 presents the mosaic in Ca II (in helioprojective representation), with photospheric and chromospheric vertical magnetic field maps and context magnetic field from an SDO HMI Active Region Patch

(SHARP; Bobra et al. 2014) in cylindrical equal-area (CEA) projection.

Imaging spectropolarimetry was obtained in the Fe I 6173 Å and Ca II 8542 Å lines. Fe I was sampled at eight different wavelengths, equidistantly distributed at 40 mÅ spacing between -0.12 Å and $+0.16 \text{ Å}$. The Ca II sampling covers $\pm 0.95 \text{ Å}$, with finer spacing in the core (down to 70 mÅ) and coarser spacing in the outer wings (up to 350 mÅ).

We used the SSTRED pipeline (de la Cruz Rodríguez et al. 2015; Löfdahl et al. 2018) to reduce the data, which includes image restoration using Multi-Object Multi-Frame Blind Deconvolution (MOMFBD; van Noort et al. 2005). Remaining small-scale seeing-induced deformations were removed according to the recipe by Henriques (2012), while further destretching to correct for rubber-sheet seeing effects was performed following Shine et al. (1994). We minimised the fringes in Stokes Q , U and V by Fourier-filtering (following the procedure in Pietrow et al. 2020) and increased the signal-to-noise (S/N) in the Ca II 8542 Å Stokes Q and U by applying the denoising neural network of Díaz Baso et al. (2019).

The mosaic was then constructed by aligning these cleaned and denoised pointings at sub-pixel accuracy through cross-correlation. To avoid sharp edge-effects from the individual pointings, we applied so-called feathering in the overlapping regions, combining the pointings according to a linear weight map that ensures a smooth transition between them. In addition, we smoothed the data across the pointing edges over a width of 10 pixels (i.e. about $0.6''$) to further reduce any remaining edge-effects. These mosaic construction steps were determined based on the Fe I and Ca II wide-band images and then applied to the respective spectropolarimetric data. Finally, we cut away two small patches at about $(X, Y) = (145'', -245'')$ and $(X, Y) = (145'', -275'')$ as both contained a strong artefact that would otherwise have led to spurious results in the inversions and as such in the lower boundary conditions for the MHS model.

CRISPEX² (Vissers & Rouppe van der Voort 2012, Löfdahl et al. 2018) was used to verify the mosaic alignment and for data browsing.

3. Magnetic field inference

3.1. Approximations for field-of-view maps

With over 2.3 million data pixels in the mosaic, performing a full-FOV non-LTE inversion would be computationally prohibitive. In order to nonetheless obtain a field-of-view estimate of the magnetic field vector we performed Milne-Eddington (ME) inversions of the Fe I data and applied a spatially-regularised weak-field approximation (WFA) to the Ca II data.

ME inversions are the workhorse of pipelines routinely delivering photospheric magnetograms for, e.g., SDO/HMI and *Hinode* SOT/SP, and (in the past) SOLIS/VSM. For our ME inversions of the SST/CRISP Fe I 6173 Å data we used *pyMilne*³, a hybrid implementation written in Python and C++ (de la Cruz Rodríguez 2019, see the upper-right panel of Fig. 1).

The WFA, on the other hand, is often used to obtain an estimate of the chromospheric magnetic field vector (e.g. de la Cruz Rodríguez et al. 2013, Pietarila et al. 2007, Harvey 2012, Kleint 2017). Here we use an extension of this method by Morosin

² <https://github.com/grviss/crispex>

³ <https://github.com/jaimedelacruz/pyMilne>

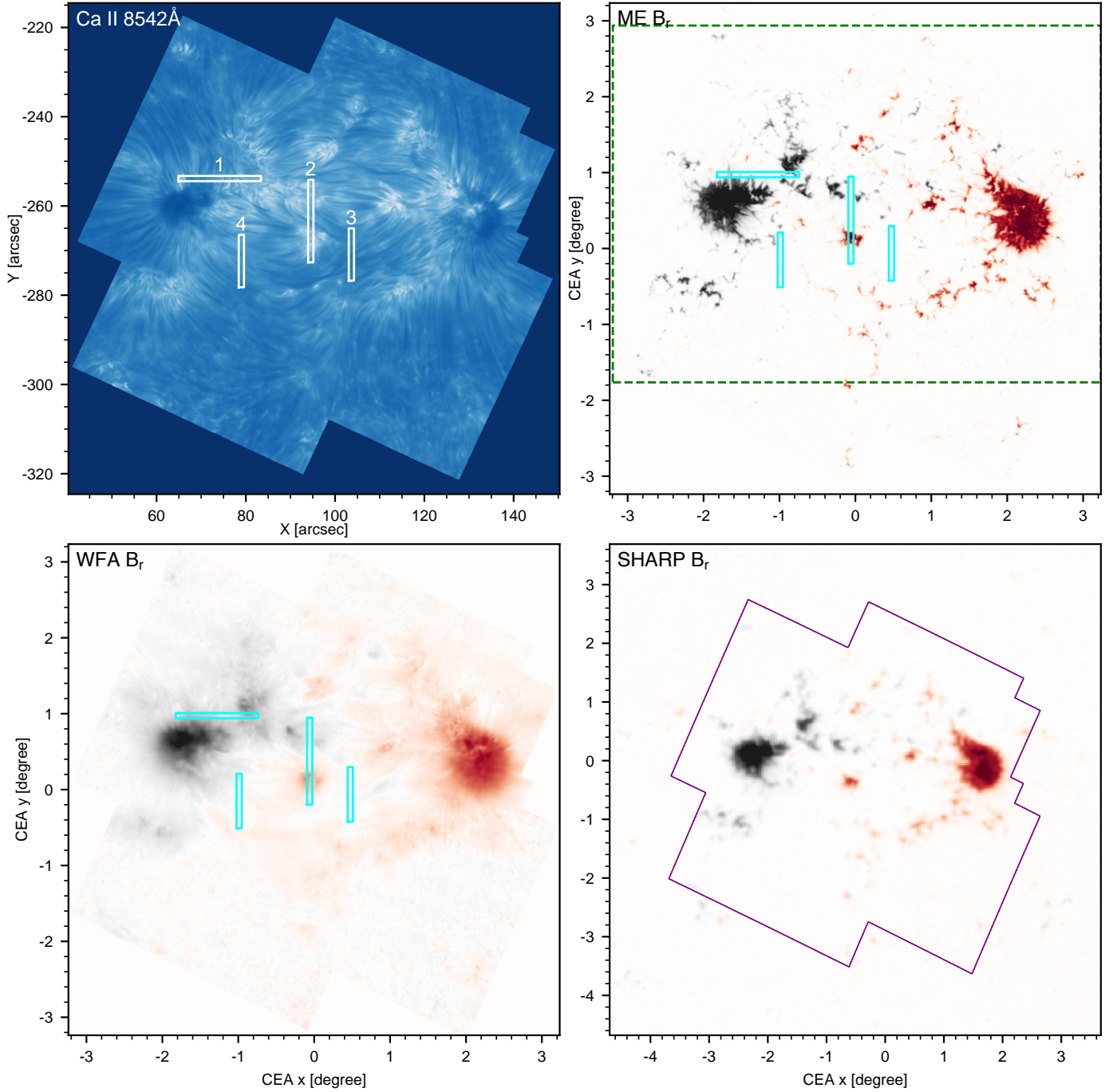


Fig. 1. SST/CRISP mosaic and context SDO/HMI-derived SHARP magnetic field of NOAA AR 12723. *Upper left:* Ca II 8542 Å line core image. *Upper right:* Milne-Eddington inferred photospheric B_r magnetic field from Fe I 6173 Å observations by SST/CRISP. *Lower left:* Chromospheric radial magnetic field B_r from the spatially-regularised weak-field approximation. *Lower right:* Same as upper right, but from SDO/HMI. The line-of-sight magnetic field maps have been clipped to ± 1.5 kG and are all reprojected and mapped to cylindrical equal-area (CEA) coordinates. The mapping to CEA precludes any direct comparison by coordinate of features in the top left panel versus the other panels. The white boxes in the top left panel indicate narrow regions-of-interest (ROIs) selected for (non-)LTE inversion and are indicated (approximately, i.e. without mapping distortion) by cyan boxes in the top right and bottom left panels. The dashed green box in the top right panel highlights the FOV selected for the magnetohydrostatic simulation, while the purple contour in the lower right panel traces the SST mosaic field-of-view.

et al. (2020), `spatial_WFA`⁴, that imposes spatial continuity in the solution and that has recently been applied with success to Ca II 8542 Å observations of an X2.2 flare (Vissers et al. 2021). The benefit of this spatially-regularised WFA is that, with well-chosen parameters, the adverse effects of noise can be greatly reduced.

⁴ https://github.com/morosinroberta/spatial_WFA

3.2. Non-LTE inversions

We also perform (non-)LTE inversions of selected regions of interest (ROIs) of our Fe I and Ca II mosaic data using the STockholm Inversion Code (STiC; de la Cruz Rodríguez et al. 2016, de la Cruz Rodríguez et al. 2019), which after settling on a best fit profile delivers an atmospheric model with (among others) temperature and velocity stratification, as well as the magnetic field

Table 1. Number of nodes used in each inversion cycle.

Cycle	Parameter				
	T	v_{los}	v_{micro}	B_{\parallel}	B_{\perp} and φ
1	4	2	0	-5.0, -0.5	-5.0, -0.5
2	6	3	2	-5.0, -0.5	-5.0, -0.5
3	9	4	3	-5.0, -2.0, -0.5	-5.0, -0.5

vector. STiC is an MPI-parallel non-LTE inversion code built around a modified version of RH (Uitenbroek 2001) to solve the atom population densities assuming statistical equilibrium and plane-parallel geometry, using an equation of state extracted from the SME code (Piskunov & Valenti 2017). We assumed complete frequency redistribution (CRD) in our inversions. The radiative transport equation is solved using cubic Bezier solvers (de la Cruz Rodríguez & Piskunov 2013). The Ca II inversions were performed in non-LTE using a 6-level calcium model atom and assuming CRD, while Fe I was treated in LTE.

We assumed FAL-C as initial model atmosphere, spanning between $\log \tau_{500} = 0.1$ and -7.1 at $\Delta \log \tau_{500} = 0.2$ spacing. For the magnetic field components B_{\parallel} , B_{\perp} and the azimuth φ we used the WFA results as initial guess. The inversions were run in three cycles, with an increased number of nodes in temperature, velocity and magnetic field for each subsequent cycle (see Table 1). Contrary to standard procedure, we inferred all three field components with two nodes already in the first cycle, as the S/N difference between Fe I and Ca II in Stokes Q , U and V otherwise tended to push the model atmosphere to a photospheric field configuration that dominated the final results. Spatial and depth smoothing between the cycles minimised the persistence of poorly fitted pixels. We present our inversion results in Section 4.3.

3.3. Azimuth disambiguation

The magnetic field azimuth φ recovered from the inference methods described in Sections 3.1 and 3.2 contains a 180° -ambiguity that needs to be resolved to determine $\mathbf{B}(x, y, z)$. Since we use the ME-inferred field as photospheric boundary condition for a magnetohydrostatic model, we resolve this ambiguity in the ME-derived photospheric azimuth according to the minimum energy method (MEM) Metcalf (1994), using the implementation by Leka et al. (2014). Regions unstable for disambiguation were identified by running twenty instances of the MEM code with different random number seeds and setting the azimuth of those pixels for which the result changed by more than 45° by majority vote.

We did, however, not attempt to disambiguate the chromospheric WFA azimuth with the same procedure as this re-introduced pixelisation of the FOV, obviating benefits from spatial regularisation. Also, given the small extent of the selected ROIs for non-LTE inversion, we did not disambiguate the inferred azimuth. In both cases we focus on the orientation, rather than the direction of the transverse field in the xy -plane.

3.4. Magnetic field decomposition and reprojection

A challenge when comparing observations with numerical experiments is that the observed quantities are projected with respect to the line-of-sight, where pixels do not all cover the same physical extent on the Sun. A common practice when using observations as boundary conditions for simulations is therefore to

reproject the observed magnetic field to cylindrical equal-area (CEA) coordinates, i.e. as if the target were observed top-down and with equally-sized pixels. Indeed, one of the formats that SHARPs can be acquired in has the magnetic field reprojected to CEA.

SolarSoft IDL⁵ provides a pipeline that delivers the HMI data in CEA coordinate projection and we have adapted this pipeline to handle SST data products. Our version is written in Python and can be found online⁶. The resulting $\mathbf{B}(r, \theta, \phi)$ maps have a 0.003° pixel-size (equivalent to about $0''.05$ at disc centre), i.e. ten times smaller than for the SHARP maps, given that the pixel size of the SST observations is about a factor 10 smaller than that of HMI. Samples of the photospheric and chromospheric B_r maps are shown in Fig. 1.

Finally, we also apply the inverse reprojection operation, i.e. from CEA back to the frame that the observations were obtained in, to facilitate comparison between the MHS model and non-LTE inversion results (given that the latter were performed in the original observations frame).

3.5. Magnetohydrostatic model

3.5.1. Model setup and boundary conditions

We use a cut-out of the ME-derived magnetic field vector in CEA coordinates (see green dashed box in Fig. 1) as lower boundary condition for a magnetohydrostatic (MHS) model of the active region, where the pixels outside the SST mosaic FOV are filled with values from the SHARP. The computational domain has $2144 \times 1568 \times 160$ pixels of 36.5 km on the side, thereby providing the field over a surface of about 78×57 Mm, for more than 5.8 Mm in height. This cut-out is well-balanced in flux, with a ratio of net-to-unsigned flux of less than 2×10^{-3} .

The MHS model (Zhu & Wiegmann 2018, 2019, Zhu et al. 2020) takes into account the interaction between the magnetic field and plasma, and is appropriate for the lower atmosphere where the plasma β (i.e. ratio of gas pressure to magnetic pressure) can be large. The model is realised in two steps. First, we initialise the magnetic field by performing a non-linear force-free field (NLFFF) extrapolation following Wiegmann (2004), based on a pre-processed version of the ME-derived magnetogram (Wiegmann et al. 2006). The plasma is initially distributed along the magnetic field lines assuming gravitational stratification. Next, the code simultaneously computes the magnetic field vector, plasma pressure and density, while iteratively minimising an objective function (Eq. (4) in Zhu & Wiegmann 2018). In this step, the original magnetogram is used as the bottom boundary condition.

3.5.2. Post-processing for comparison with inversions

Comparing the MHS model results to the non-LTE inversions of selected ROIs (or WFA of the full field) requires post-processing, since the MHS field maps are in CEA coordinates and geometrical z -height scale, rather than in helioprojective Cartesian (X, Y) and optical depth $\log \tau_{500}$. Firstly, we therefore reproject the MHS magnetic field back to the same frame as the observations, using the inverse operation. Secondly, we extract the chromospheric magnetic field at equivalent heights in the MHS model and the non-LTE-inferred atmospheres. To that end, we inspect the response functions of Ca II 8542 Å Stokes Q , U

⁵ <http://www.lmsal.com/solarsoft>

⁶ See the remap utility package in <https://github.com/ISP-SST/ISPy>

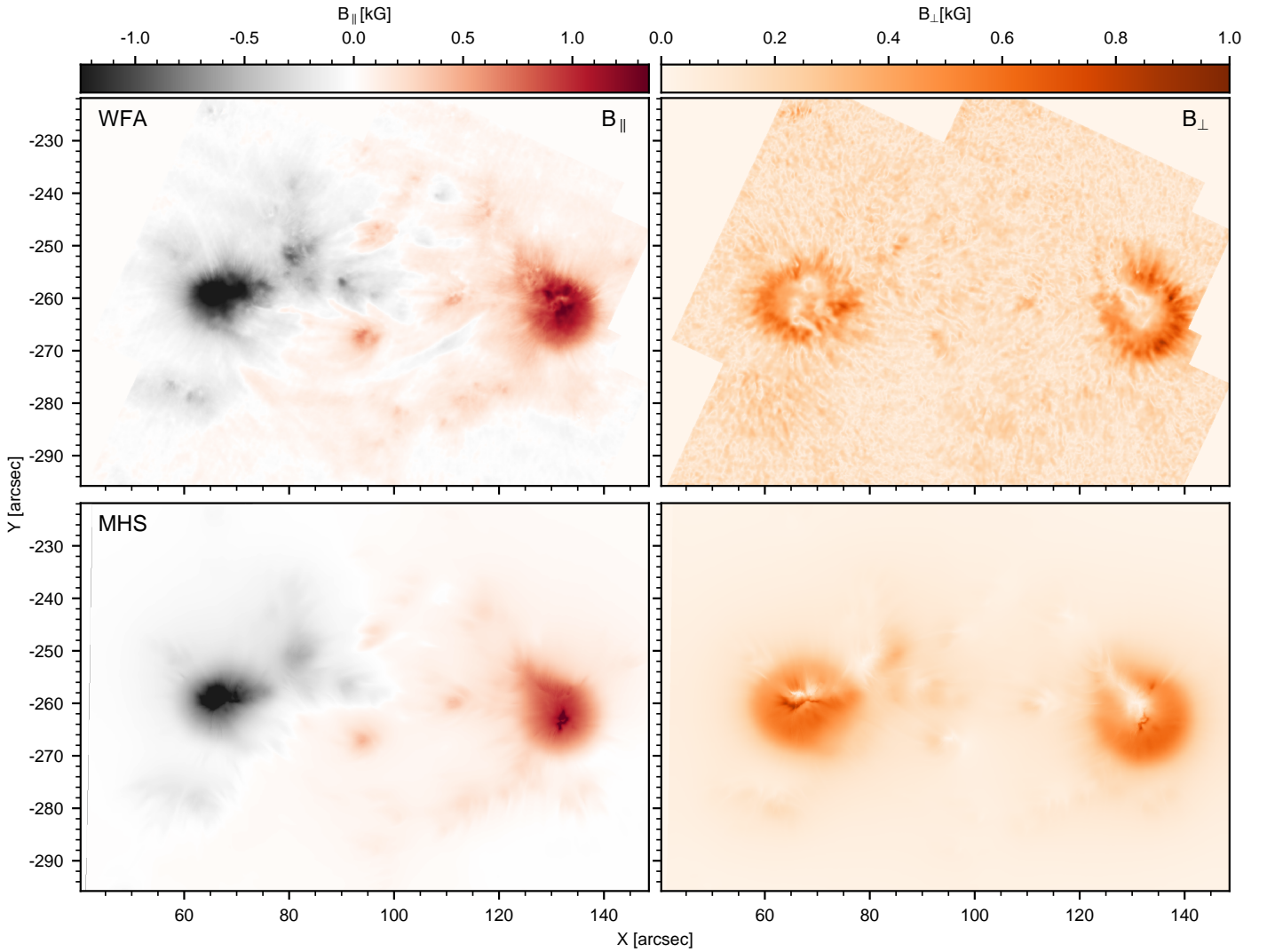


Fig. 2. Magnetic field components B_{\parallel} (left) and B_{\perp} (right) from the WFA (top row) and from the MHS model (bottom row), averaged over the equivalent height range (as determined from the column mass) that the WFA is expected to be sensitive to. To allow direct comparison between the WFA and MHS results, the panels in each column have been clipped to the same values: between $[-1.35, 1.25]$ kG for B_{\parallel} and $[0, 1]$ kG for B_{\perp} . In addition, the B_{\parallel} panels (left column) have been gamma-adjusted to improve visibility of weaker features.

and V for all ROIs, finding that the highest sensitivity in Q and U to changes in B_{\perp} and in V to changes in B_{\parallel} is reached between $\log \tau_{500} = -4.1$ and -5.1 . For our top-down views of the chromospheric field we therefore average the inferred magnetic field components over this range and determine the column mass equivalent to those $\log \tau_{500}$ -depths, which in turn yields the column mass depths to average over in the MHS model. In addition, we recompute the zero point of the column-by-column hydrostatic z -scale in the inferred atmospheres by imposing horizontal gas pressure equilibrium (including magnetic pressure) in both the x - and y -direction at the continuum $\tau_{500} = 1$ depth, shifting the z -scale of each column in the ROI accordingly. This procedure follows the one outlined in Section 4.3 of Morosin et al. (2020). As pointed out in that study, this is necessarily only an approximation as we cannot include the Lorentz force or magnetic pressure in our inversions. Thirdly, and finally, as the MHS azimuth covers the full 360° circle, while our WFA and inversion results retain a 180° -ambiguity, we introduce this ambiguity in the MHS result by subtracting 180° from any azimuth equal to or greater than 180° , so that the azimuth maps can be compared side-by-side.

4. The chromospheric magnetic field in AR 12723

An important question is whether the MHS model can reproduce the chromospheric field, solely based on the photospheric boundary condition provided by the ME inversion of our Fe I data. To evaluate the degree of similarity, we compare the MHS results both on active region scales with the spatially-regularised WFA field (Sections 4.1 and 4.2) and in closer detail for selected regions-of-interest that we inverted in non-LTE (Section 4.3). While we inverted four ROIs, we focus on the two most interesting ones, ROIs 1 and 3 in the main part of this publication and include discussion of ROIs 2 and 4 in Appendix A.

4.1. Magnitude of the magnetic field components

The WFA provides the three magnetic field components over a corrugated surface in z -scale that depends on the location within the field-of-view, which we need to take into account when comparing with the MHS field. As described in Section 3.5.2, we determine the column mass equivalent to $\log \tau_{500} = -4.1$ and -5.1 and use those boundaries to select the column mass depths

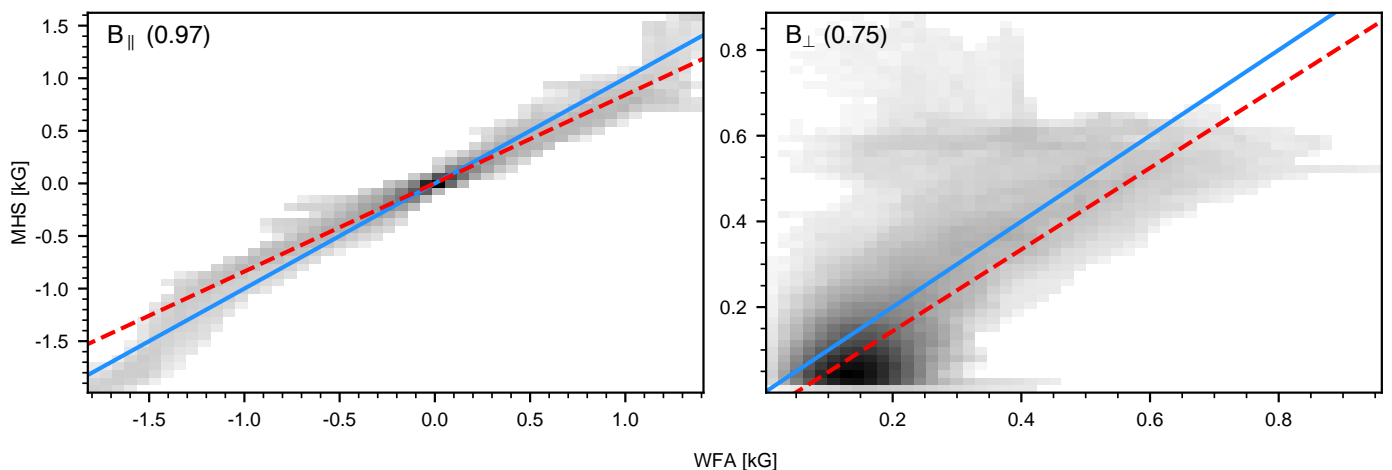


Fig. 3. Two-dimensional histograms of the WFA versus MHS magnetic field for B_{\parallel} (left) and B_{\perp} (right) for the overlapping part of the FOV shown in Fig. 2 (i.e. excluding pixels without Ca II data). The diagonal blue line indicates a 1:1 relationship, while the dashed red line shows a linear fit to the data.

over which to average in the MHS model. Figure 2 compares the B_{\parallel} and B_{\perp} maps from the spatially-regularised WFA and the resulting depth-averaged MHS model.

Qualitatively, there is good agreement for the strongest field concentrations, both in B_{\parallel} and B_{\perp} , however much of the substructure that the WFA recovers in e.g. the superpenumbra of both sunspots, appears more as a homogeneous and comparatively weaker-field haze in the MHS panels. For instance, the strong B_{\parallel} inside the sunspots is more extended in the WFA results, especially for the positive-polarity sunspot, and elongated strong-field concentrations are seen to extend radially from both sunspots in the WFA B_{\perp} that are entirely absent in the MHS.

Meanwhile, the stronger field concentrations outside the sunspots in the WFA B_{\parallel} are only recovered in location in the MHS B_{\parallel} , but weaker in strength and hardly in terms of fine-structure. The lack of magnetic features outside the sunspots in the MHS model is particularly striking when comparing both B_{\perp} panels (right-hand column), although much of the fine-structure in the WFA B_{\perp} in the lower right of the FOV (i.e. left of $X = 80''$ and below $Y = -280''$) is likely spurious as suggested by weak total linear polarisation in those areas. As such, the MHS B_{\perp} field does a good job in identifying locations with significant horizontal chromospheric field. Another feature of interest is the band of negative B_{\parallel} around $(X, Y) = (110'', -270'')$ in the WFA panel, that coincides with dark elongated fibrils as seen in the Ca II line core (cf. e.g. Fig. 1 top left panel). While it is only visible weakly because of its much smaller field strength compared to the sunspots, it is evidently absent in the MHS panel. We consider these high fibrils in further detail in Section 4.3.2.

Figure 3 compares the WFA and MHS magnetic field components quantitatively in two-dimensional histograms. For B_{\parallel} (left-hand panel) the correlation is generally tight, as also evidenced by the Pearson correlation number of 0.97, and indeed for weak field strengths (below 0.2–0.3 kG) this correlation appears to be essentially one-to-one. For larger field strengths the scatter cloud widens and overall tends to lower field strengths in the MHS compared to the WFA, as indicated by the linear regression (dashed red line). Considering B_{\perp} (right-hand panel) the scatter cloud is much wider and while the WFA-recovered field strengths are generally larger than in the MHS model (i.e. the darkest parts of the two-dimensional histogram are found right of the one-to-one line), there is an extended cloud of points at WFA field strengths below 0.5 kG that exceed that value by some

0.35–0.70 kG in the MHS model. These points correspond to the spuriously looking narrow field enhancements in both sunspot centres in the MHS B_{\perp} map. Careful examination of the data suggests that these regions appear as a result of data processing and become pronounced only after averaging in height. So, despite the wider scatter and offset by about +100 G in favour of the WFA, the linear regression has a slope of 0.96, indicating an essentially 1:1 relationship between the WFA and MHS in B_{\perp} .

4.2. Chromospheric field azimuth and fibril orientation

As the chromosphere is a low- β regime where the magnetic pressure dominates in the pressure balance, the fibrils visible in e.g. the Ca II 8542 Å line core are expected to be relatively well-aligned with the local magnetic field vector, even though the extent to which this is the case may vary depending on target and local conditions (e.g. de la Cruz Rodríguez & Socas-Navarro 2011, Schad et al. 2013, 2015, Leenaarts et al. 2015, Zhu et al. 2016, Martínez-Sykora et al. 2016, Asensio Ramos et al. 2017, Jafarzadeh et al. 2017, Bjørgen et al. 2019). Figure 4 shows the azimuth φ derived from the WFA in yellow and from the MHS model in red overlaid on an unsharp masked (with radius 0.5) Ca II line core intensity image of AR 12723. The MHS azimuth is obtained by averaging over the column mass range equivalent to $\log \tau_{500} = -4.1$ to -5.1 (see Section 3.5.2). Given that we did not disambiguate the WFA azimuth (see also Section 3.3) and since we are primarily interested in comparing the fibril orientation with the field azimuth, we omit all arrowheads in the Fig. 4 overlays.

Considering the full FOV (panel A), the WFA azimuth agrees well with both the MHS azimuth and the orientation of fibrillar structures in the superpenumbra of both sunspots, as well as the fibrils in parts of the inter-spot region (e.g. above and to the right of box C). Moving away from the sunspot centres and the stronger field-concentrations and pores, the WFA azimuth disagrees more often with the fibril orientation, e.g. in part of the superpenumbra of the negative-polarity sunspot (above and to the very left of box B), the fibrils connected to bright plage south of that spot (to the lower left of box D) and notably for the dark fibril around $(X, Y) = (128'', -245'')$, to the north of the positive-polarity sunspot. In contrast, the MHS azimuth is relatively well-aligned with the fibrils also at greater distance from

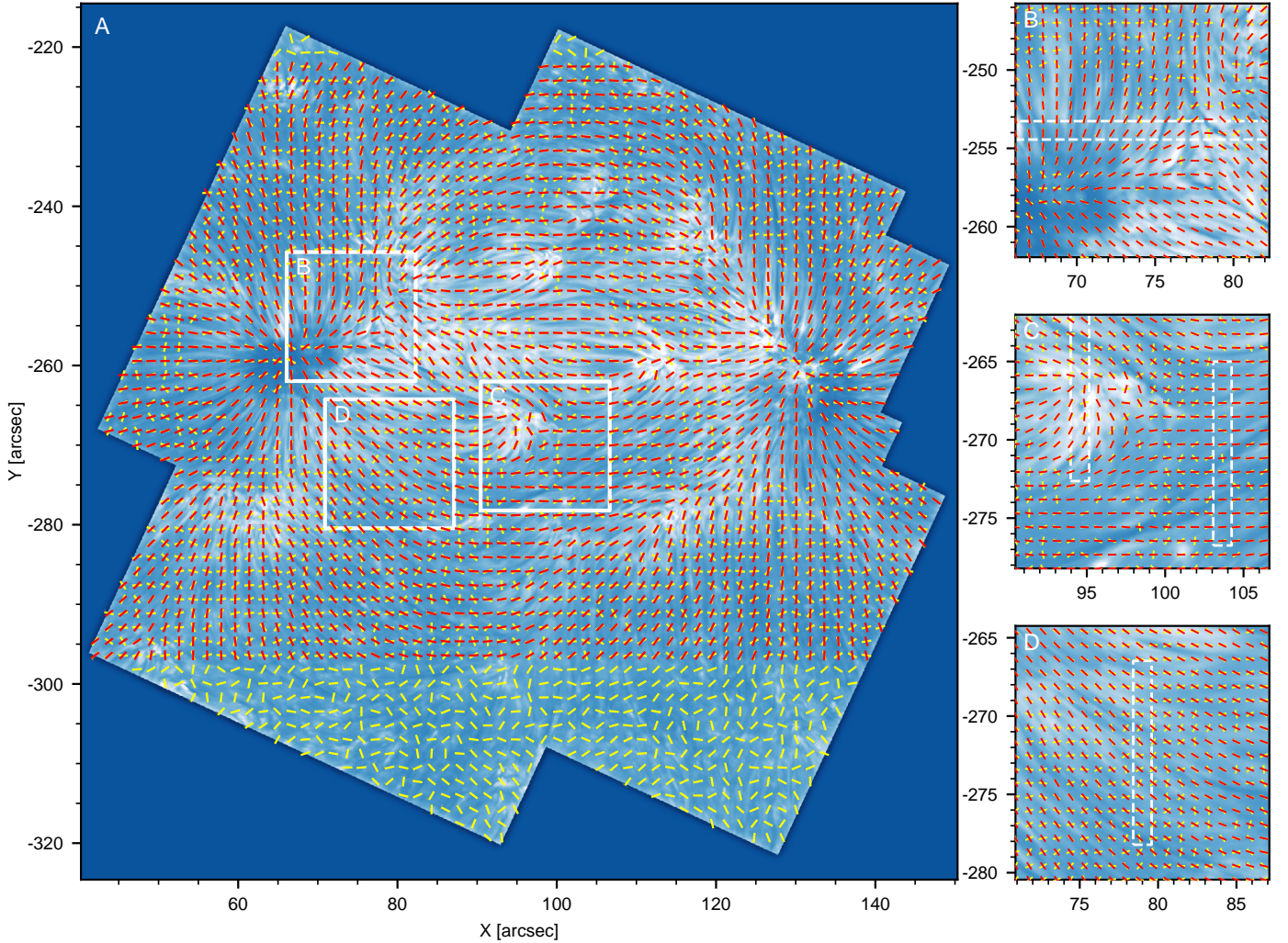


Fig. 4. Comparison of fibril orientation and chromospheric field azimuth from the spatially-regularised WFA and the MHS model. The background Ca II 8542 Å image has been unsharp masked with a radius of 0.5 to enhance fibrillar structures. The azimuth is indicated by yellow (WFA) and red (MHS) bars, where arrowheads have been omitted since we did not resolve the 180°-ambiguity for the WFA. The three white boxes in the left-hand panel (a) indicate the selections presented as panels (b)–(d) in the right-hand column and have been chosen such as to contain part of the ROIs in Fig. 1, where panel (b) covers ROI 1, panel (c) ROIs 2 and 3, and panel (d) ROI 4.

the sunspots (especially around the left-hand negative-polarity sunspot and aforementioned dark fibril north of the positive-polarity sunspot), which in turn means the WFA and MHS azimuth more often cross at near-perpendicular angles. At the same time, the orientation of a long fibril that extends from the positive-polarity sunspot into box C appears not to be captured in the MHS model (the azimuth bars are essentially parallel to the x -axis) while the WFA azimuth is better aligned with this fibril at several places. Finally, outside the strong-field areas of the active region (e.g. in the bottom, lower right and upper left parts of the mosaic FOV) the WFA azimuth is more random, but the lack of clear fibrillar structures also renders a comparison in these regions less straightforward. A source of this randomness is that the WFA will always provide an azimuth as output, even if the linear polarization signal is completely dominated by noise.

Figure 4b–d zoom in on three cutout boxes of about $16'' \times 16''$ marked B–D in Fig. 4a. Cutout B covers part of the negative-polarity sunspot and its superpenumbra, as well as the ROI 1 box (indicated by dashed white lines), cutout C a magnetic concentration in the inter-spot region (including ROIs 2 and 3) and cutout D the superpenumbra south of the negative-polarity sunspot (including ROI 4). These detailed views paint a sim-

ilar picture as the FOV overview, in that the WFA azimuth is often well-aligned with Ca II fibrils at or in the vicinity of strong field (e.g. dark fibrils close to the sunspot in cutout B, fibrils extending to the south from the positive-polarity pore around $(X, Y) = (94'', -270'')$ and those that cross the lower right quadrant of the box (between about $(X, Y) = (93'', -278'')$ and $(X, Y) = (106'', -269'')$) in cutout C, upper left part of cutout D (between $(X, Y) = (80'', -270'')$ and the upper left corner), but the mis-alignment increases when moving away from sunspot or pore (e.g. top 3'' of cutout B, fibrils north of the pore in cutout C, most of cutout D except for the upper left quadrant). In contrast, the MHS azimuth more often traces the fibrils over larger parts of these sub-FOVs, with the notable and aforementioned exception of the long dark fibrils crossing the lower right quadrant of cutout C.

4.3. Detailed comparison of selected regions-of-interest

4.3.1. ROI 1: Sunspot vicinity

Figure 5 presents a comparison of the observations, inversions and modelling results for the detailed view of ROI 1, just north

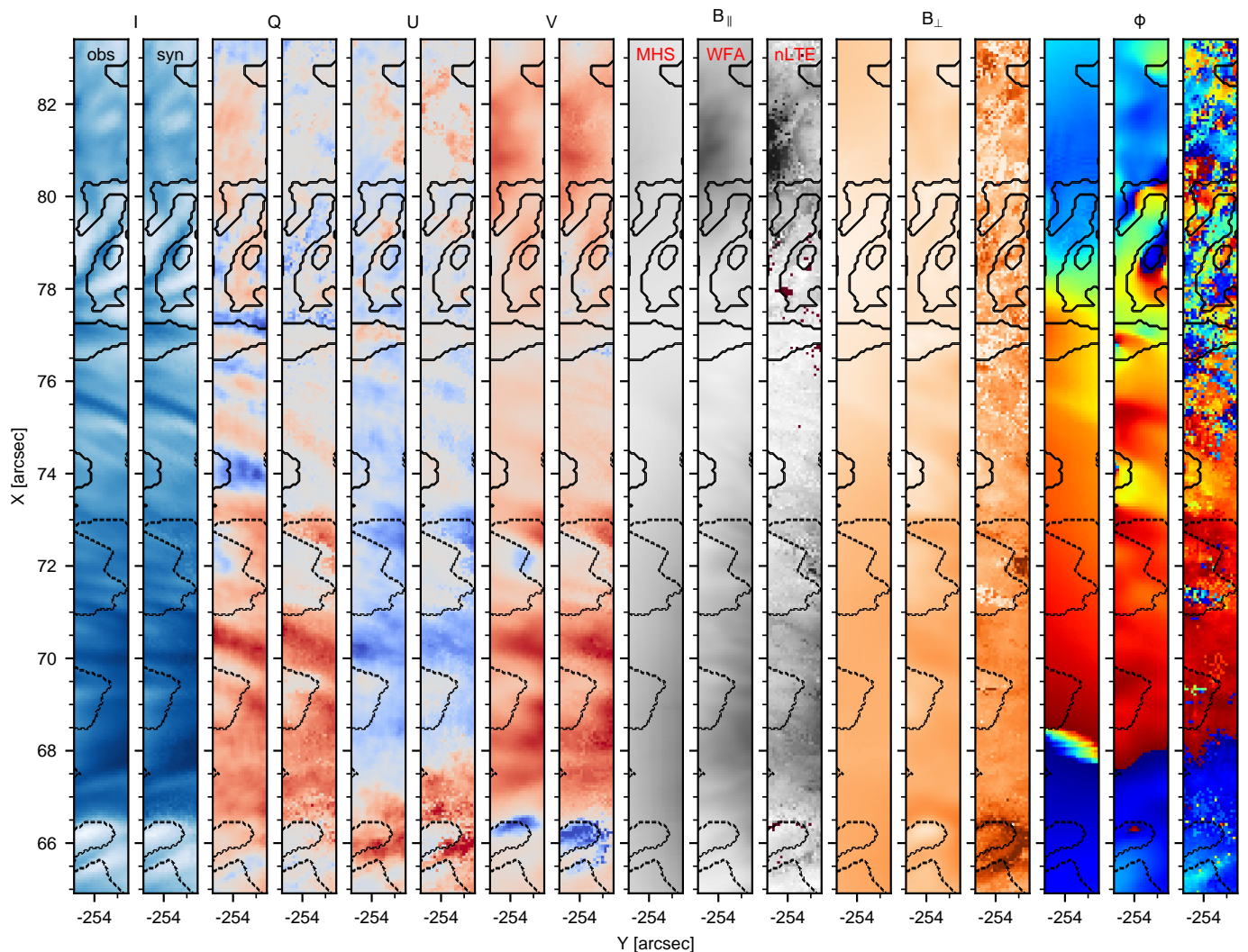


Fig. 5. Maps of Stokes intensity and magnetic field components for ROI 1. The ROI has been rotated by 90° counter-clockwise to allow for an identical layout as Figs. 7, A.1 and A.3. The first eight columns contain the Stokes I , Q , U and V intensity maps, where each column pair shows first the observed and then the synthetic maps, clipped to the same values. The Stokes I map is taken at $\text{Ca II } 8542 \text{ \AA}$ line centre, while the other Stokes components are shown at $\Delta\lambda = +0.21 \text{ \AA}$ offset. The remaining nine columns contain the magnetic field components B_{\parallel} , B_{\perp} and azimuth ϕ , where each column triple shows from left to right the MHS, WFA and non-LTE inversion result, again clipped to the same values. The non-LTE magnetic field components are the average over $\log \tau_{500} = [-5.1, -4.1]$, while the MHS field components are averaged over the equivalent z -height (determined per pixel). The contours highlight regions where the WFA-derived B_{\perp} transitions 150 G (solid) and 350 G (dashed). The tick spacing is the same for both the x - and y -axes.

of the negative polarity sunspot. The first eight columns compare the intensity maps in all four Stokes components from the observations and best fits as determined by the non-LTE inversions and serve primarily to assess the quality of the inferred model atmosphere. The remaining nine columns show the B_{\parallel} , B_{\perp} and ϕ from the MHS model, WFA and non-LTE STiC inversions. The contours in all panels highlight the regions where the WFA-derived B_{\perp} reaches 150 G (solid contours) and 350 G (dashed). As the ROI has been rotated counter-clockwise by 90° , the Solar- X axis lies along the vertical axis and the sunspot lies to the right of these cut-outs, up to about $X = 74''$.

The magnetic field maps have been averaged over $\log \tau_{500} = -4.1$ and -5.1 , since inspection of the response functions of Ca II Stokes Q , U and V indicates maximum sensitivity to the magnetic field in that $\log \tau_{500}$ -depth range. The MHS maps are averaged over the equivalent range in column mass, as derived from the non-LTE inversions (see Section 3.5.2).

Comparing the observed and synthetic maps, we see that especially Stokes I and in general also V are well-reproduced. The synthetic map for the latter contains locations where strong signal is more extended compared to the observations (e.g. the blue patch around $X = 66''$), but also places where signal is lacking (e.g. around $X = 72''$). This translates into B_{\parallel} maps that in their general distribution of field concentrations are essentially the same between the MHS model, WFA results and the non-LTE inversions. However, both the WFA and especially the non-LTE inversions return stronger field in the chromosphere, e.g. close to the sunspot (between $X = 66''$ and $73''$) and between $X = 80''$ and $82''$.

The non-LTE inversions struggle somewhat more for Stokes Q and U , though mostly where the horizontal field is expected to be weak (based on the WFA). For instance, within the contour lines centred at $X = 77''.5$, where the WFA-derived B_{\perp} is less than 150 G, and in general above $X = 80''.5$ the synthetic maps hardly recover any signal even though the observed

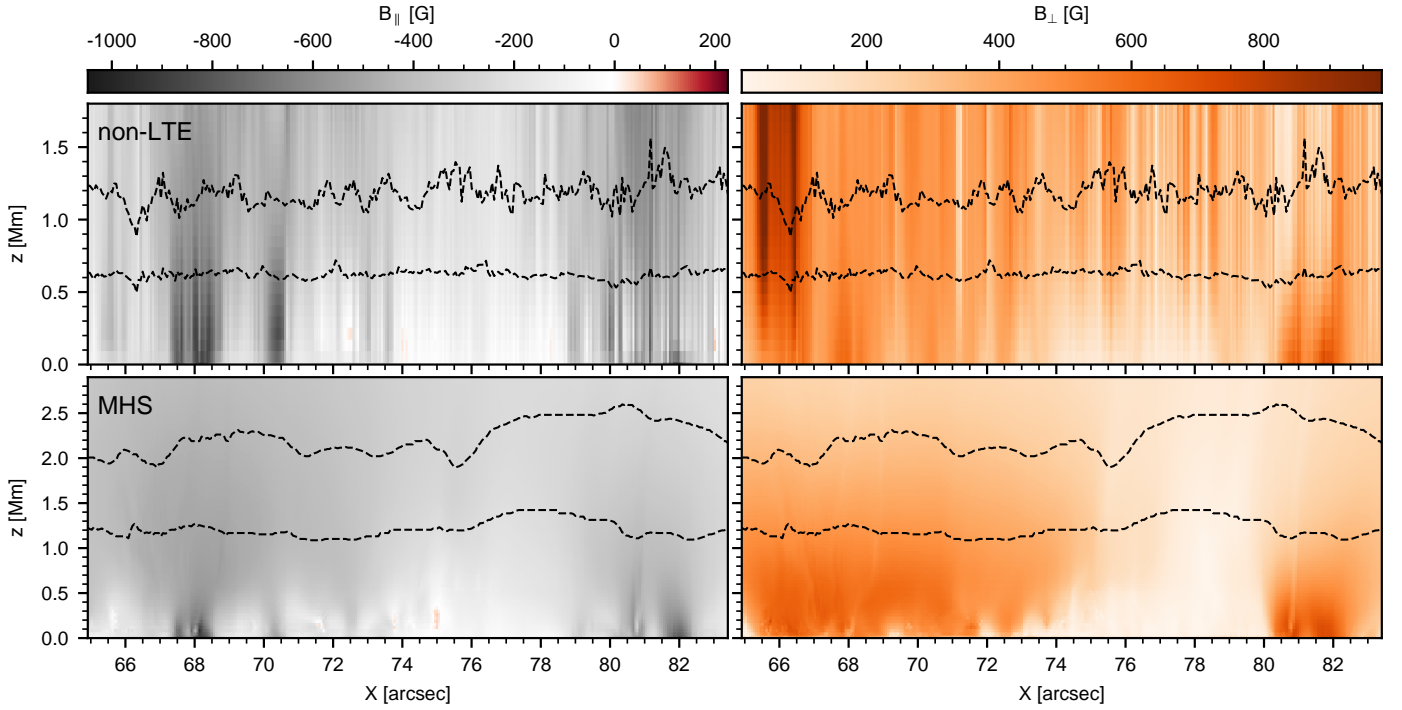


Fig. 6. Vertical cuts in B_{\parallel} (left column) and B_{\perp} (right column). The cuts have been taken along the long axis of ROI 1, averaging over the central 5 pixels across that axis. *Top row:* non-LTE-inferred field. *Bottom row:* MHS field. The non-LTE and MHS panels have been clipped to the same values according to the colour bars at the top of the figure. The dashed lines indicate the heights corresponding to $\log \tau_{500} = -5.1$ (upper line) and -4.1 (lower line) in the upper panels and the equivalent column mass in the MHS model in the lower panels, where the latter panels also show the field over a larger z -height range than in the top row.

maps clearly exhibit some structure. This is reflected in both the inferred B_{\perp} and φ maps, that are particularly noisy between $X = 75''$ and $83''$.

Figure 6 shows vertical cuts in B_{\parallel} and B_{\perp} along the long axis of ROI 1, averaged over the central 5 pixels across that axis, for both the non-LTE-inferred field and the MHS field. The dashed lines indicate the equivalent $\log \tau_{500} = -4.1$ and -5.1 depths over which the field has been averaged for display in Fig. 5, where the $\log \tau_{500} = -5.1$ depth is more corrugated than $\log \tau_{500} = -4.1$, especially in the inversions (upper row). Both the B_{\parallel} and B_{\perp} cuts look very similar between the non-LTE inversions and the MHS model. There are B_{\parallel} field concentrations rooted at $z = 0$ Mm around $X = 68''$, $70.5''$ and $82''$, although the non-LTE inversions have the strong field extending further and persist between about 0.6–1.2 Mm, while the MHS field exhibits a much more diffuse distribution at those heights. Similarly, the B_{\perp} cuts have a pair of stronger field concentrations around $X = 80.5''$ and $82''$ that in both cases extend up to about $z = 0.6$ Mm in the non-LTE panel and slightly lower in the MHS panel. The marked difference is stronger transverse field above 0.5 Mm between $X = 65''$ and $67''$ for the non-LTE inversions, that is absent in the MHS model. Finally, the lower atmosphere (up to about 0.5–0.6 Mm in the non-LTE case and up to about 1 Mm in the MHS case) between $X = 74''$ and $79''$ exhibits close-to-zero B_{\parallel} and B_{\perp} field strengths in both the inversions and MHS model.

4.3.2. ROI 3: High fibrils

Figures 7 and 8 present the results for ROI 3 in the same format as Figs. 5–6 for ROI 1. The location for ROI 3 was chosen for its crossing of a set of the longest fibrils in our mosaic observations, that are evident as dark slanted bands around $Y = -272''$

in Stokes I (Fig. 7, first two columns). Stokes V is particularly strong at the location of these fibrils, which is reflected in a seemingly homogeneous band of strong negative polarity in both WFA- and non-LTE-inferred B_{\parallel} maps. While both Stokes Q and U show structure in their signature at this location, the correlation with the dark bands in Stokes I is not evident. Still, the WFA recovers B_{\perp} in excess of 150 G in a patch overlapping with the strongest negative B_{\parallel} at the location of these fibrils (cf. contours at $Y = -272''$).

Unsurprisingly, the non-LTE inversions struggle in reproducing the Q and U profiles in the areas where the WFA already suggests the transverse field is weaker (cf. the $B_{\perp} = 150$ G contours, for instance between $Y = -274.5''$ and $-272.5''$ and between $Y = -272''$ and $Y = -269''$), while the stronger field contour-enclosed areas typically show a similar amount of structure between the observed and synthetic Q and U maps. Notwithstanding, the non-LTE B_{\perp} agrees qualitatively with the WFA-inferred B_{\perp} for most of the sub-FOV, albeit with more noise. The same holds for the azimuth φ , with the exception of several smaller patches that are found in either the WFA or non-LTE inversions (e.g. the blue-red patch at $Y = -271.5''$ in the WFA azimuth that is not at all well-defined in the non-LTE results).

One stark difference when comparing the field from different methods, is that the MHS results show little to no field structuring at the $\log \tau_{500}$ -equivalent heights used to construct these maps, in contrast to ROI 1 (and to some extent also ROI 2, see Appendix A.1). In particular, the strong B_{\parallel} (and to certain extent B_{\perp}) associated with the dark fibrils in the Ca II line core intensity image is absent in the MHS model and instead the MHS field components exhibit little to no structure. These discrepancies are also reflected in the vertical cross-cuts shown in Fig. 8, where at the height of the horizontal cuts (i.e. between the dashed lines) the MHS model exhibits a weakly positive B_{\parallel} of less than 30 G

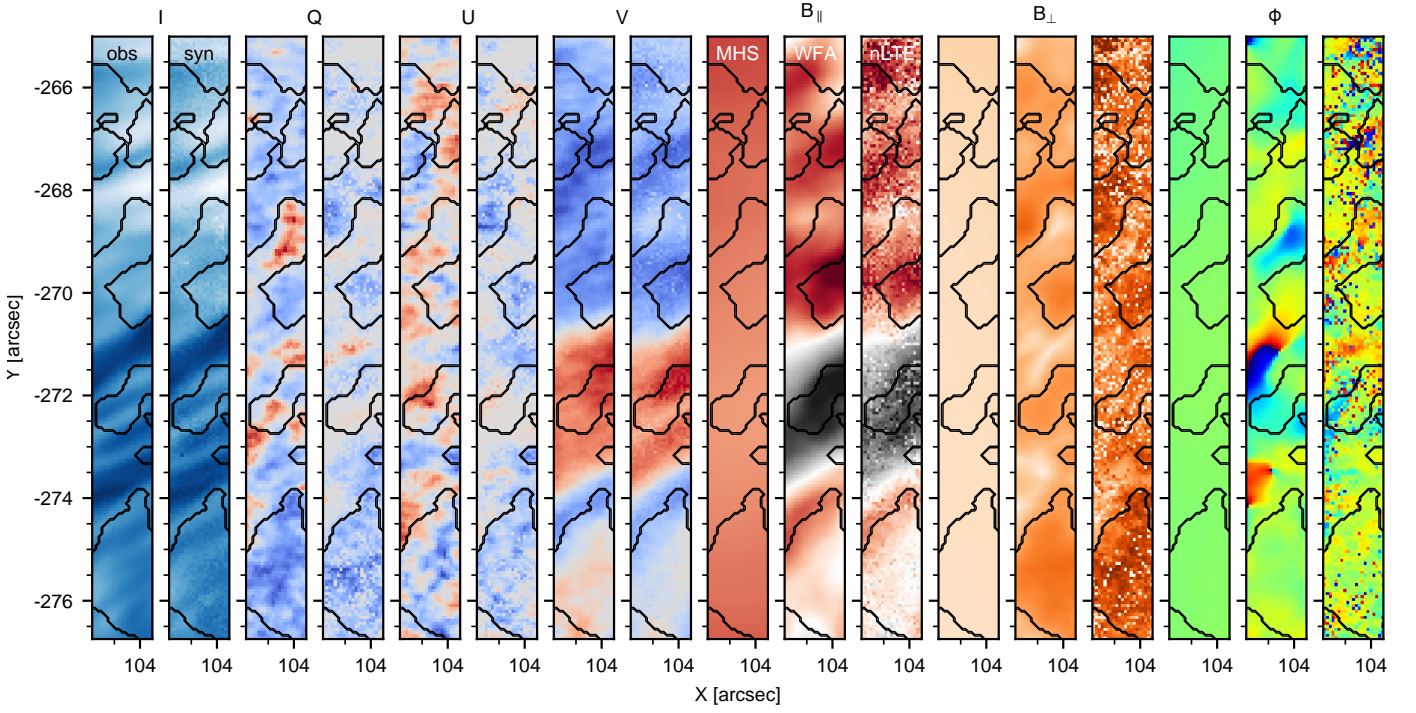


Fig. 7. Maps of Stokes intensity and magnetic field components for ROI 3. Format as for Fig. 5, except that contours are only shown for $B_{\perp} = 150$ G in the WFA-derived field.

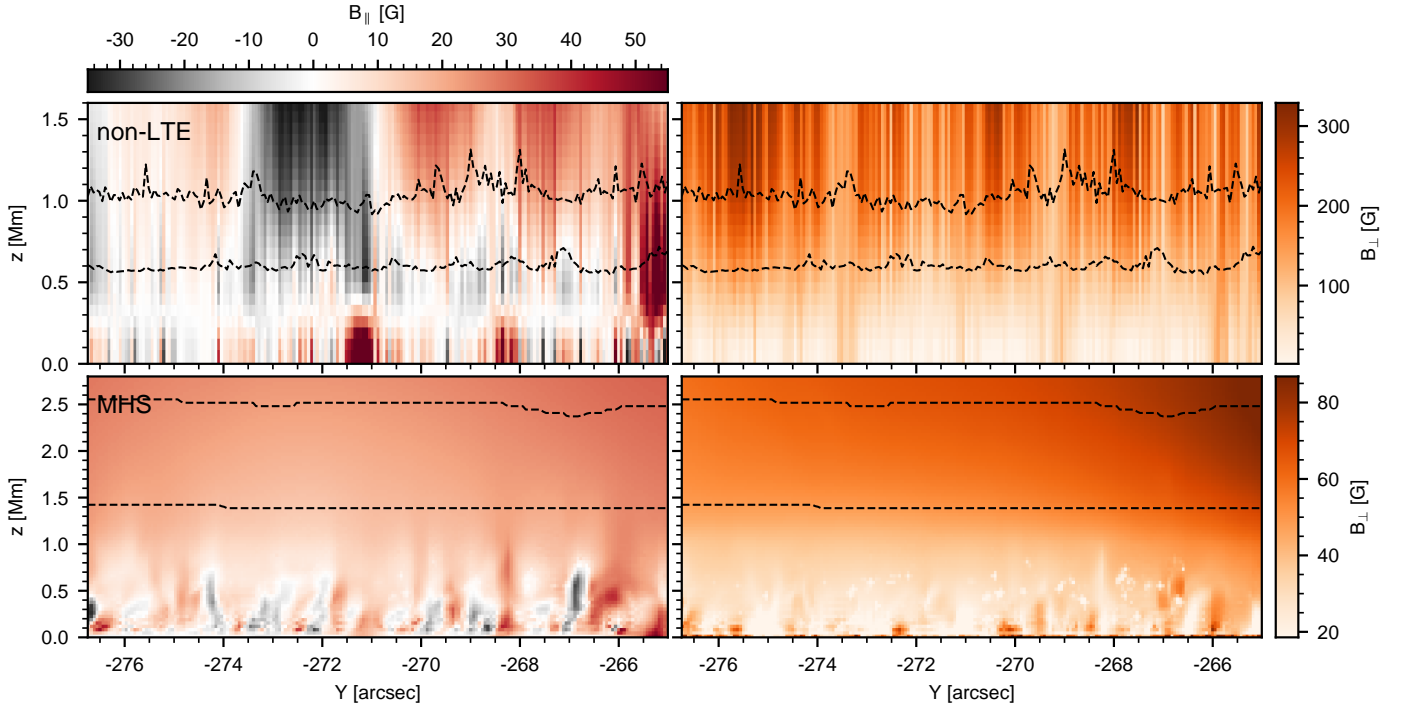


Fig. 8. Vertical cuts in B_{\parallel} (left column) and B_{\perp} (right column) for ROI 3. Format as for Fig. 6, except that the B_{\perp} panels (right column) have been clipped individually, according to the colour bars on the right of the figure.

and B_{\perp} below 80 G in the strongest-field part around $Y = -266''$. While at the equivalent $\log \tau_{500}$ -depths the non-LTE-inferred B_{\parallel} is only barely stronger in absolute terms compared to the MHS results, B_{\perp} is stronger by up to a factor 5 in the top right non-LTE panel.

Lower down in the atmosphere, below 500 km, the alternating positive and negative B_{\parallel} polarities in the MHS panel, and in particular their extensions to 700–800 km, are not always

as well-recovered in the non-LTE results. However, careful inspection shows that most of the stronger-field concentrations at heights 0–200 km are located at approximately the same place in both panels, albeit typically with larger field strengths in the non-LTE case, e.g. the positive polarities at $Y = -273''8$, $-272''5$, between $-271''5$ and $-271''$, and between $-268''5$ and $-268''$, or the negative polarities at $Y = -276''$, near $-274''$ and $-267''7$.

A similar structuring of alternating stronger and weaker B_{\perp} along the vertical cut is found in the lower atmosphere of the MHS model, while the non-LTE cut only shows the stronger concentrations of those, e.g. at $-273''5$, $-269''$ and $-266''$. It turns out the inversions of Fe I struggled, especially for Stokes Q and U . Higher up in the atmosphere, above about 1 Mm, the results diverge even further, with a B_{\perp} concentration in excess of 300 G in the non-LTE panel around $Y = -276''$, while the MHS B_{\perp} is a factor 5–6 weaker at equivalent column mass. On the other hand, the B_{\perp} values in the upper right corner differ only by up to a factor 2 and are often even quite close between non-LTE and MHS results.

5. Discussion

5.1. Chromospheric magnetic field on active region scales

Qualitatively, the MHS and WFA field agree in spatial distribution of the stronger-field concentrations, i.e. sunspots and pores, but the WFA shows more enhanced field fine-structure (cf. Fig. 2), which can be most clearly seen for the transverse component in the superpenumbra of either sunspot. While a contribution from the photosphere could conceivably play a role, it is unlikely the case here as both Stokes Q and U exhibit this strong-signal superpenumbral fine-structure already in the first off-core wavelength samplings and the restricted wavelength range chosen to determine the WFA with would furthermore minimise any photospheric contribution.

Quantitatively, B_{\parallel} exhibits a tighter correlated between the WFA and MHS model than B_{\perp} , while the latter is closer to a one-to-one relationship, yet in both cases the WFA field strengths tend to be larger than in the MHS model. This tendency can easily be understood by considering the maps in Fig. 2, which show a much more extended region of strong-field B_{\parallel} for the sunspots in the WFA map than in the MHS map, especially for the positive-polarity sunspot. Similarly, the strongest enhancements in B_{\perp} are found for the superpenumbral substructure in the WFA map, while the MHS exhibits a much smoother spatial distribution, except for enhanced field crossing the sunspot centres (which is data processing artefacts). The latter have no counterpart in the WFA map, explaining the scatter cloud in the top left of the right-hand panel in Fig. 3, while the former are the reason for the majority of the distribution lying to the right of the one-to-one diagonal.

On large scales the MHS azimuth appears to follow the Ca II 8542 Å fibril structures more closely than the WFA azimuth does and this is particularly so outside the sunspots and pores. There the Ca II Stokes Q and U signals are weak and noisy, leading to weaker and more uncertain inferred transverse field strengths and azimuths, and the visible misalignment between fibrils and WFA azimuth could therefore, at least in part, be attributable to the signal-to-noise ratio of the underlying observations. However, whether the inferred field should follow the line-core fibril structures may depend on the target. For instance, de la Cruz Rodríguez & Socas-Navarro (2011) found most of the derived azimuths to be consistent with the fibril orientation in two targets observed with Ca II 8542 Å spectropolarimetry. Similarly, Schad et al. (2013), found the inferred field orientation to be well-aligned with the projected angles of the fibrils, to within an error of only 10° , and Asensio Ramos et al. (2017) report alignment to within about 16° for the superpenumbra, although the misalignment could be up to about 34° in magnetically weaker plage regions. We observe a qualitatively similar effect, in that the WFA azimuth appears to trace the dark super-

penumbral fibrils reasonably well, but is more often at odds with fibrils outside the stronger-field concentrations.

5.2. Magnetic field from non-LTE inversions

In general, the non-LTE inversions recover a similar spatial distribution of the chromospheric field as the WFA, in particular for the B_{\parallel} component, but to a decent extent also for B_{\perp} (at least where the transverse field is relatively strong). Unsurprisingly though, the inversions struggle to derive clean maps for B_{\perp} wherever Stokes Q and/or U are relatively noisy (e.g. ROIs 3 and 4 in Figs. 7 and A.3, respectively). Despite the spatially-regularised WFA having served as initial guess, the B_{\perp} maps for ROIs 3 and 4 (and in part also ROI 2) are far from smooth and this carries over into the non-LTE-inferred azimuth that for most of those FOVs disagrees with the WFA-derived azimuth even in a broad sense (cf. Figs. A.1 and A.3 for ROIs 2 and 4, respectively). One reason for the increased noise is that in order for non-LTE inversions to work, the stratification of all parameters must be inferred correctly, not only the magnetic field. This leads to more degenerate solutions and hence more noise in the inferred parameters.

Of all ROIs, the first shows the highest degree of similarity between the MHS, WFA and non-LTE inversions for all three magnetic field components. ROI 2 comes a close second, at least for B_{\parallel} and B_{\perp} , while ROIs 3 and 4 differ considerably in most aspects. Indeed, while all four ROIs exhibit similar photospheric patterns between the MHS model and non-LTE inversions in the vertical cross-cuts for B_{\parallel} and B_{\perp} , the MHS B_{\perp} field strengths in ROIs 3 and 4 are up to a factor 5 smaller at chromospheric heights than what the non-LTE inversions indicate. This can be understood from the proximity to strong-field concentrations for ROIs 1 and 2 persisting from the photosphere to greater heights (cf. the vertical cross-cuts in Figs. 6 and A.2), in contrast to ROIs 3 and 4 that are located in more ‘quiet’ parts of the FOV. Given that the MHS model extrapolates from the photospheric field, it will inherently exhibit a better agreement at chromospheric heights in the vicinity of strong-field concentrations than in magnetically weaker regions.

Also, despite the large difference in transverse chromospheric field strengths in the ‘quiet’ ROIs, the distribution of weaker field in the photosphere and stronger field in the chromosphere is qualitatively similar between the MHS model and non-LTE inversions. This pattern can be explained by the difference in origin of the field. In the lower atmosphere the field comes from the (weak) photospheric polarities, while the field higher up is that connecting the active region’s main polarities. As such, both the MHS model and non-LTE inversions present a similar magnetic field stratification of the active region’s connectivity, only that the latter recovers stronger transverse field in the chromosphere.

Evidently, ROI 3 presents a further discrepancy that cannot be explained in a similar way. Here, both the WFA and non-LTE inversions pick up on the enhanced Ca II 8542 Å Stokes polarisation corresponding to the dark fibrils traversing this sub-field, while the MHS model shows essentially a smooth extension from the upper-photospheric field state. Despite that these dark fibrils appear to connect both sunspots and are thus expectedly rooted in either of the main polarities in the photosphere, the MHS model is unable to reproduce the magnetic imprint thereof at chromospheric heights.

6. Conclusions

We have presented an analysis of the chromospheric magnetic field in AR 12723 as inferred with a spatially-regularised weak-field approximation and a non-LTE inversion code, and compared these against a magnetohydrostatic model based solely on the photospheric vector magnetic field. We find that the chromospheric field is qualitatively similar between these methods, where the line-of-sight component is best reproduced in the MHS model, while the transverse component is consistently weaker than the WFA-derived field, especially outside the sunspots. In general, the MHS model also presents a smoother field component maps than the WFA, despite the spatial regularisation applied in the latter, and while the MHS model is unable to recover the magnetic imprint in B_{\parallel} and B_{\perp} from a set of long fibrils that appear to connect both sunspots, there is otherwise remarkably good agreement with the WFA.

In addition, the vertical cuts in magnetic field offer a similar view in the MHS model and non-LTE inversions, especially for the two ROIs that are close to the stronger field concentrations (i.e. the negative-polarity sunspot and crossing the pores) and at least qualitatively for the ROIs that are taken in more “quiet” parts of the field-of-view, albeit in some places with transverse field strengths up to a factor 5 or so weaker than in the non-LTE inversions or WFA. On the other hand, the non-LTE inversions struggle in recovering the transverse component when its strength is below some 200–300 G. For the more quiet ROIs the non-LTE inversions also appear to “overshoot” and settle on stronger B_{\perp} than the WFA indicates, even though the Stokes Q and U are not always recovered in magnitude. The noisiness of the non-LTE-inferred B_{\perp} and φ maps in contrast to those from the spatially-regularised WFA further emphasises the need for spatial coupling in the inversions as proposed in recent years by Asensio Ramos & de la Cruz Rodríguez 2015, de la Cruz Rodríguez 2019).

While the MHS model agrees qualitatively (and to a large extent quantitatively) with the observationally inferred chromospheric field, it does not retrieve all the features from the observations and our results therefore support earlier studies which indicate that including a chromospheric constraint in field extrapolations or data-driven modelling can improve the recovery of chromospheric and coronal magnetic structures. In particular the difficulty in reaching a transverse chromospheric field strength similar to that observationally inferred or recovering the presence of high fibrils suggests that key ingredients may thus still be missed, whereas an accurate estimate of the chromospheric field within, for instance, erupting flux ropes is vital to properly predict the geo-effectiveness of earth-bound CMEs (Kilpua et al. 2019).

Acknowledgements. GV has been supported by a grant from the Swedish Civil Contingencies Agency (MSB). This research has received funding from the European Union’s Horizon 2020 research and innovation programme under grant agreement No 824135. JL and SD are supported by a grant from the Knut and Alice Wallenberg foundation (2016.0019). XZ is supported by the mobility program (M-0068) of the Sino-German Science Center. This project has received funding from the European Research Council (ERC) under the European Union’s Horizon 2020 research and innovation programme (SUNMAG, grant agreement 759548). This project has received funding from the European Research Council (ERC) under the European Union’s Horizon 2020 research and innovation programme (SolMAG, grant agreement No 724391). The Institute for Solar Physics is supported by a grant for research infrastructures of national importance from the Swedish Research Council (registration number 2017-00625). The Swedish 1-m Solar Telescope is operated on the island of La Palma by the Institute for Solar Physics of Stockholm University in the Spanish Observatorio del Roque de los Muchachos of the Instituto de Astrofísica de Canarias. The SDO/HMI data used are courtesy of NASA/SDO and HMI science team. The inversions were performed on resources provided by the Swedish National Infrastructure

for Computing (SNIC) at the National Supercomputer Centre at Linköping University. We made much use of NASA’s Astrophysics Data System Bibliographic Services. Last but not least, we acknowledge the community effort to develop open-source packages used in this work: *numpy* (Oliphant 2006; numpy.org), *matplotlib* (Hunter 2007; matplotlib.org), *scipy* (Virtanen et al. 2019; scipy.org), *astropy* (Astropy Collaboration et al. 2013, Price-Whelan et al. 2018; astropy.org), *sunpy* (The SunPy Community et al. 2020; sunpy.org), *scikit-learn* (Pedregosa et al. 2011; scikit-learn.org).

References

- Asensio Ramos, A. & de la Cruz Rodríguez, J. 2015, *A&A*, 577, A140
 Asensio Ramos, A., de la Cruz Rodríguez, J., Martínez González, M. J., & Socas-Navarro, H. 2017, *A&A*, 599, A133
 Astropy Collaboration, Robitaille, T. P., Tollerud, E. J., et al. 2013, *A&A*, 558, A33
 Bjørgen, J. P., Leenaarts, J., Rempel, M., et al. 2019, *A&A*, 631, A33
 Bobra, M. G., Sun, X., Hoeksema, J. T., et al. 2014, *Sol. Phys.*, 289, 3549
 de la Cruz Rodríguez, J. 2019, *A&A*, 631, A153
 de la Cruz Rodríguez, J., Leenaarts, J., & Asensio Ramos, A. 2016, *ApJ*, 830, L30
 de la Cruz Rodríguez, J., Leenaarts, J., Danilovic, S., & Uitenbroek, H. 2019, *A&A*, 623, A74
 de la Cruz Rodríguez, J., Löfdahl, M. G., Sütterlin, P., Hillberg, T., & Rouppe van der Voort, L. 2015, *A&A*, 573, A40
 de la Cruz Rodríguez, J. & Piskunov, N. 2013, *ApJ*, 764, 33
 de la Cruz Rodríguez, J., Rouppe van der Voort, L., Socas-Navarro, H., & van Noort, M. 2013, *A&A*, 556, A115
 de la Cruz Rodríguez, J. & Socas-Navarro, H. 2011, *A&A*, 527, L8
 De Rosa, M. L., Schrijver, C. J., Barnes, G., et al. 2009, *ApJ*, 696, 1780
 Díaz Baso, C. J., de la Cruz Rodríguez, J., & Danilovic, S. 2019, *A&A*, 629, A99
 Fleishman, G., Mysh’akov, I., Stupishin, A., Loukitcheva, M., & Anfinogentov, S. 2019, *ApJ*, 870, 101
 Hammerschlag, R. H., Sliepen, G., Bettonvil, F. C. M., et al. 2013, *Optical Engineering*, 52, 081603
 Harvey, J. W. 2012, *Sol. Phys.*, 280, 69
 Henriques, V. M. J. 2012, *A&A*, 548, A114
 Hunter, J. D. 2007, *Computing in Science & Engineering*, 9, 90
 Jafarzadeh, S., Rutten, R. J., Solanki, S. K., et al. 2017, *ApJS*, 229, 11
 Jin, M., Schrijver, C. J., Cheung, M. C. M., et al. 2016, *ApJ*, 820, 16
 Keller, C. U., Harvey, J. W., & Giampapa, M. S. 2003, in *Society of Photo-Optical Instrumentation Engineers (SPIE) Conference Series*, Vol. 4853, *Innovative Telescopes and Instrumentation for Solar Astrophysics*, ed. S. L. Keil & S. V. Avakyan, 194–204
 Kilpua, E. K. J., Lugaz, N., Mays, M. L., & Temmer, M. 2019, *Space Weather*, 17, 498
 Kleint, L. 2017, *ApJ*, 834, 26
 Leenaarts, J., Carlsson, M., & Rouppe van der Voort, L. 2015, *ApJ*, 802, 136
 Leka, K. D., Barnes, G., & Crouch, A. 2014, *AMBIG: Automated Ambiguity-Resolution Code*
 Lemen, J. R., Title, A. M., Akin, D. J., et al. 2012, *Sol. Phys.*, 275, 17
 Löfdahl, M. G., Hillberg, T., de la Cruz Rodríguez, J., et al. 2018, *arXiv e-prints*, arXiv:1804.03030
 Martínez-Sykora, J., De Pontieu, B., Carlsson, M., & Hansteen, V. 2016, *ApJ*, 831, L1
 Metcalf, T. R. 1994, *Sol. Phys.*, 155, 235
 Metcalf, T. R., De Rosa, M. L., Schrijver, C. J., et al. 2008, *Sol. Phys.*, 247, 269
 Morosin, R., de la Cruz Rodríguez, J., Vissers, G. J. M., & Yadav, R. 2020, *A&A*, 642, A210
 Oliphant, T. E. 2006, *A guide to NumPy*, Vol. 1 (Trelgol Publishing USA)
 Pedregosa, F., Varoquaux, G., Gramfort, A., et al. 2011, *Journal of Machine Learning Research*, 12, 2825
 Pesnell, W. D., Thompson, B. J., & Chamberlin, P. C. 2012, *Sol. Phys.*, 275, 3
 Pietarila, A., Socas-Navarro, H., & Bogdan, T. 2007, *ApJ*, 663, 1386
 Pietrow, A. G. M., Kiselman, D., de la Cruz Rodríguez, J., et al. 2020, *A&A*, 644, A43
 Piskunov, N. & Valenti, J. A. 2017, *A&A*, 597, A16
 Price, D. J., Pomoell, J., & Kilpua, E. K. J. 2020, *A&A*, 644, A28
 Price-Whelan, A. M., Sipőcz, B. M., Günther, H. M., et al. 2018, *AJ*, 156, 123
 Reardon, K. P. & Cauzzi, G. 2012, in *American Astronomical Society Meeting Abstracts*, Vol. 220, *American Astronomical Society Meeting Abstracts #220*, 201.11
 Schad, T. A., Penn, M. J., & Lin, H. 2013, *ApJ*, 768, 111
 Schad, T. A., Penn, M. J., Lin, H., & Tritschler, A. 2015, *Sol. Phys.*, 290, 1607
 Scharmer, G. 2017, in *SOLARNET IV: The Physics of the Sun from the Interior to the Outer Atmosphere*, 85

- Scharmer, G. B., Bjelksjo, K., Korhonen, T. K., Lindberg, B., & Petterson, B. 2003, Society of Photo-Optical Instrumentation Engineers (SPIE) Conference Series, Vol. 4853, The 1-meter Swedish solar telescope, ed. S. L. Keil & S. V. Avakyan, 341–350
- Scharmer, G. B., Narayan, G., Hillberg, T., et al. 2008, *ApJ*, 689, L69
- Scherrer, P. H., Schou, J., Bush, R. I., et al. 2012, *Sol. Phys.*, 275, 207
- Schou, J., Scherrer, P. H., Bush, R. I., et al. 2012, *Sol. Phys.*, 275, 229
- Scullion, E., Rouppe van der Voort, L., Wedemeyer, S., & Antolin, P. 2014, *ApJ*, 797, 36
- Shine, R. A., Title, A. M., Tarbell, T. D., et al. 1994, *ApJ*, 430, 413
- The SunPy Community, Barnes, W. T., Bobra, M. G., et al. 2020, *The Astrophysical Journal*, 890, 68
- Toriumi, S., Takasao, S., Cheung, M. C. M., et al. 2020, *ApJ*, 890, 103
- Uitenbroek, H. 2001, *ApJ*, 557, 389
- van Noort, M., Rouppe van der Voort, L., & Löfdahl, M. G. 2005, *Sol. Phys.*, 228, 191
- Virtanen, P., Gommers, R., Oliphant, T. E., et al. 2019, *arXiv e-prints*, arXiv:1907.10121
- Vissers, G. & Rouppe van der Voort, L. 2012, *ApJ*, 750, 22
- Vissers, G. J. M., Danilovic, S., de la Cruz Rodríguez, J., et al. 2021, *A&A*, 645, A1
- Wiegmann, T. 2004, *Sol. Phys.*, 219, 87
- Wiegmann, T., Inhester, B., & Sakurai, T. 2006, *Sol. Phys.*, 233, 215
- Wiegmann, T., Thalmann, J. K., Schrijver, C. J., De Rosa, M. L., & Metcalf, T. R. 2008, *Sol. Phys.*, 247, 249
- Zhu, X., Wang, H., Du, Z., & He, H. 2016, *ApJ*, 826, 51
- Zhu, X. & Wiegmann, T. 2018, *ApJ*, 866, 130
- Zhu, X. & Wiegmann, T. 2019, *A&A*, 631, A162
- Zhu, X., Wiegmann, T., & Solanki, S. K. 2020, *A&A*, 640, A103

Appendix A: Additional regions of interest

In this Appendix we present the results for additional regions of interest, in similar format as for ROIs 1 and 3.

Appendix A.1: ROI 2: Pore and strong-field concentrations

The figure pair Fig. A.1 and A.2 presents the results for ROI 2 in a similar format as Figs. 5 and 6, only with the contours in Fig. A.1 now indicating solely the $B_{\perp} = 150$ G level. Similar to ROI 1, Stokes I and V are in general best-reproduced, while Q and U are more problematic, especially where the WFA already indicates that the field is weak. For instance, the regions to the right of the contours around $(X, Y) = (95'', -266'')$, the band around $Y = -264''$, or within the contours around $Y = -262''$ are mostly devoid of signal in the synthetic Q and U maps. Surprisingly, this is also the case for that part of the ROI below the contour around $Y = -264''$, where the WFA returned stronger B_{\perp} and one could have expected a similar result as above the contour at $Y = -262''$ and to the left of those crossing the vertical edges at $Y = -259''.5$ and $-257''.5$, where much of the structure in linear polarisation is reproduced.

This ROI crosses a positive polarity pore around $Y = -267''$ and another stronger field concentration around $Y = -256''$, as is evident from the B_{\parallel} maps in both Figs. A.1 and A.2. Especially around the pore, both MHS, WFA and non-LTE inversions agree in the top-down viewed shape of the positive polarity, although the non-LTE inversions suggest much stronger field at those heights than either the WFA and especially the MHS results. Also, where the WFA and non-LTE inversions return strong negative B_{\parallel} (i.e. around $Y = -258''$ and especially $-256''$), there no such significant concentration in the MHS model. Looking for the same locations in the vertical cut, we find that the MHS model does have marked B_{\parallel} field concentrations at those Y locations, yet already strongly attenuated at heights equivalent to $\log \tau_{500} = -4.1$ (lower dashed line) and field strengths of some 500–600 G above the pore and -100 G around $Y = -256''$. In contrast, the non-LTE inversions have field strengths of, respectively, order 800 G and -200 G persisting above $\log \tau_{500} = -4.1$. In both cases, B_{\parallel} is strongly vertical above the positive polarity pore, but somewhat more inclined with height in the MHS model for the negative polarity.

The transverse field shows the strongest concentrations at the location of the pore, only extending a few hundred kms in height in the MHS model and reduced to some 200–300 G between the $\log \tau_{500} = -4.1$ and -5.1 lines, while the non-LTE inversions exhibit B_{\parallel} in excess of 400 G around $Y = -267''.5$. For most of the vertical cut, both non-LTE inversions and MHS model exhibit weak B_{\perp} field.

Where the azimuth for ROI 1 is largely similar between MHS, WFA and non-LTE inversions for most of that sub-FOV, this is not the case for ROI 2 (last three columns of Fig. A.1). Indeed, although we find some resemblance between MHS and WFA azimuths south of about $Y = -268''$, only few other spots in the FOV are anywhere near agreement (e.g. close to $Y = -260''.5$, $-258''$ or $-254''.5$). Noise dominates the non-LTE azimuth, although with some effort similar patterns as in the WFA azimuth can be found south of $Y = -269''$, between the contours at $Y = -263''.5$ and $-263''$, between $Y = 260''.5$ and $-258''.5$ and north of $Y = -255''.5$.

Appendix A.2: ROI 4: Fibrils in sunspot vicinity

Finally, Figs. A.3 and A.4 present the results for a region covering some of the longer fibrils extending to the south-west of the negative-polarity sunspot. Similar to ROI 3, Stokes Q and U are again best reproduced where the WFA indicates $B_{\perp} \geq 150$ G (dark orange within contours in the middle B_{\perp} panel), although the magnitude of the signal is not always reproduced (e.g. red in Stokes U at $Y = -275''.5$ or blue in the same panel but around $-267''.5$). Outside these contours, little signal is found in the synthetic Q and U profiles and this explains the noisiness of the B_{\perp} and φ at those locations. Within the stronger- B_{\perp} contours the non-LTE-inferred B_{\perp} and φ appear more homogeneous, with the former reaching larger field strengths than in the WFA, while the corresponding φ panels show largely the same angle in those places, except within the contour at $Y = -271''$. Interestingly, the non-LTE azimuth much more clearly resembles the WFA results compared to ROI 2, even though the B_{\perp} magnitudes between the two ROIs are similar.

The MHS model exhibits much weaker field throughout, of the order of the weaker field in the WFA cut, although qualitatively it agrees in having stronger B_{\perp} in the upper part of the ROI, north of about $Y = -270''$. This is also reflected in the vertical cross-cut (Fig. A.4, right column), showing an area of stronger field in the upper right corner of the cross-cut for both non-LTE inversions and MHS model. The B_{\perp} in the lower atmosphere shows little resemblance between the two, however, except maybe the location of a region of stronger B_{\perp} around $Y = -272''$, albeit with a much smaller extent in the MHS model. Finally, the MHS azimuth φ (Fig. A.3, third column from the right) is nowhere near close that of the WFA or non-LTE inversions.

Meanwhile, Stokes V is largely reproduced, except some of the details around $Y = -270''$ and $-267''$, yet this seems to have little effect on the determined B_{\parallel} when compared to the WFA. The contrast with the MHS B_{\parallel} is evident, however. The band of near-zero negative polarity recovered in the WFA and non-LTE inversions between $Y = -275''.5$ and $-271''.5$ (correlating with a likewise weakly positive Stokes V signal) is positive in the MHS model and the stronger negative polarity in the former two around $-267''$ is barely negative in the MHS model. The vertical cross-cut (Fig. A.4, left column) shows the latter is because of a transition from positive to negative polarity where a strong positive field concentration extending over roughly 1 Mm and into the bottom part of the height range used for the maps in Fig. A.3. Also, any sign of a band of weak negative B_{\parallel} left of $Y = -271''.5$ is missing in the MHS model. On the other hand, the B_{\parallel} in the lower atmosphere of the non-LTE inversions bears some similarity to that in the MHS results, at least left of about $Y = -270''$. Even though generally not agreeing in magnitude and often not in (vertical) extent either, the negative polarity concentrations close to $Y = -278''$, $-277''.5$, and near $-270''$, as well as the positive concentrations between $Y = -274''.5$ and $-271''.5$ or the alternating positive-negative concentrations between $Y = -271''.5$ and $-270''$ are similar between the two panels.

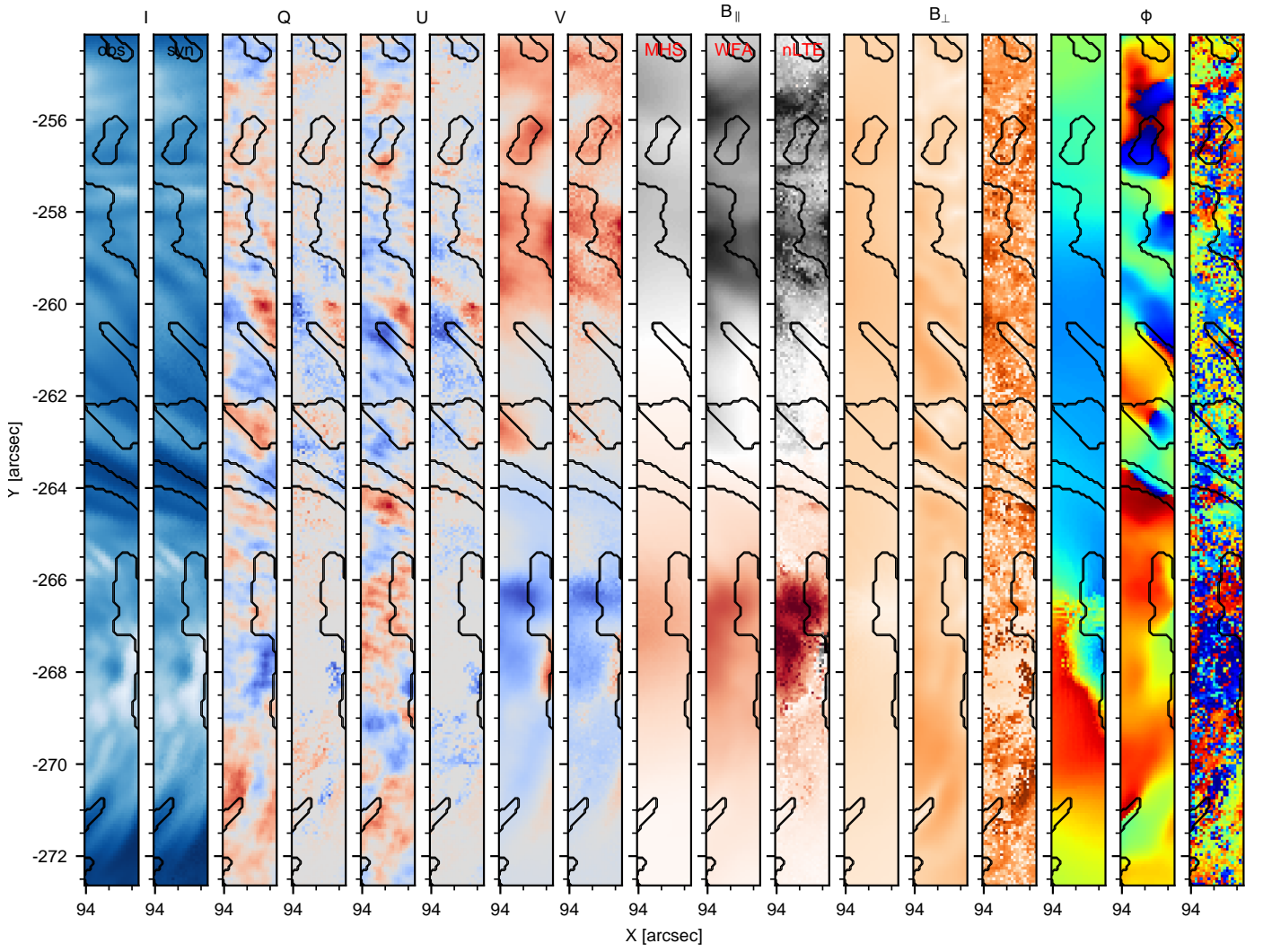


Fig. A.1. Maps of Stokes intensity and magnetic field components for ROI 2. Format as for Fig. 5, except that the contours now only show the WFA-derived $B_{\perp} = 150$ G boundary.

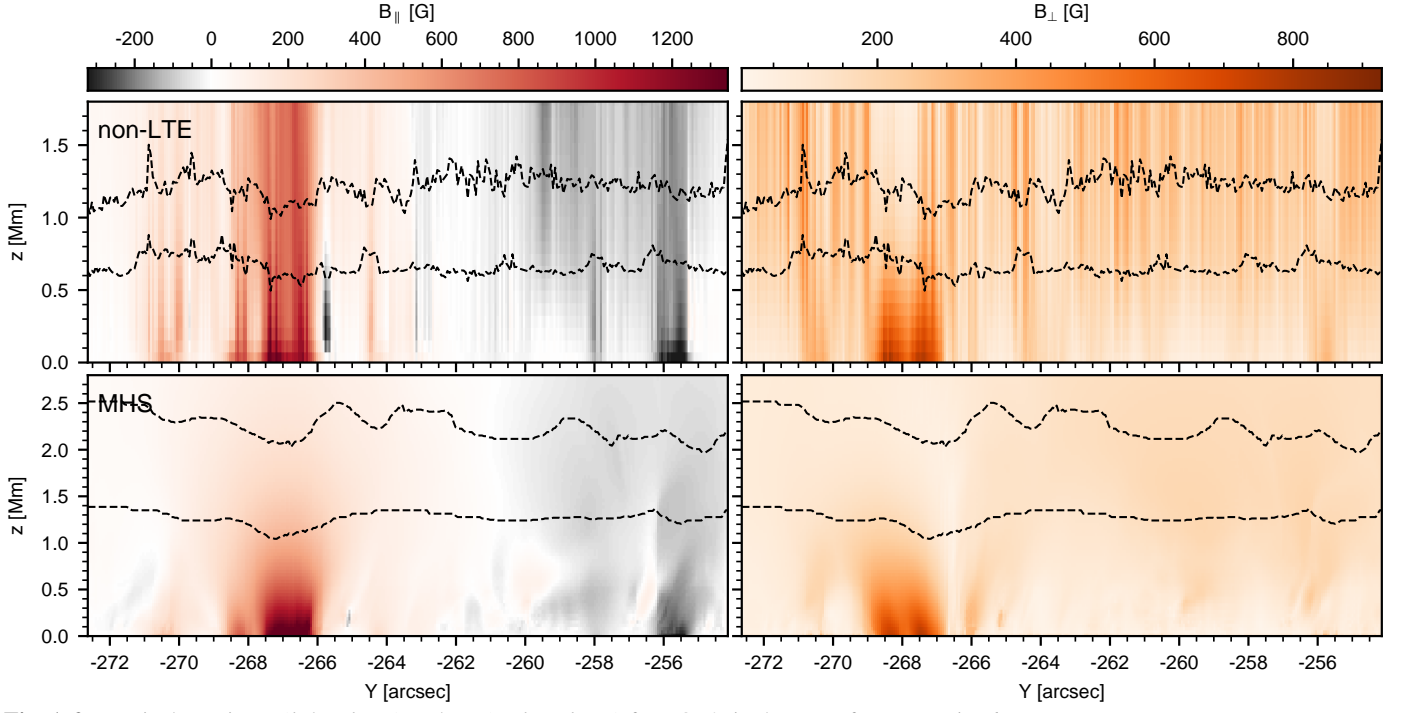


Fig. A.2. Vertical cuts in B_{\parallel} (left column) and B_{\perp} (right column) for ROI 2, in the same format as Fig. 6.

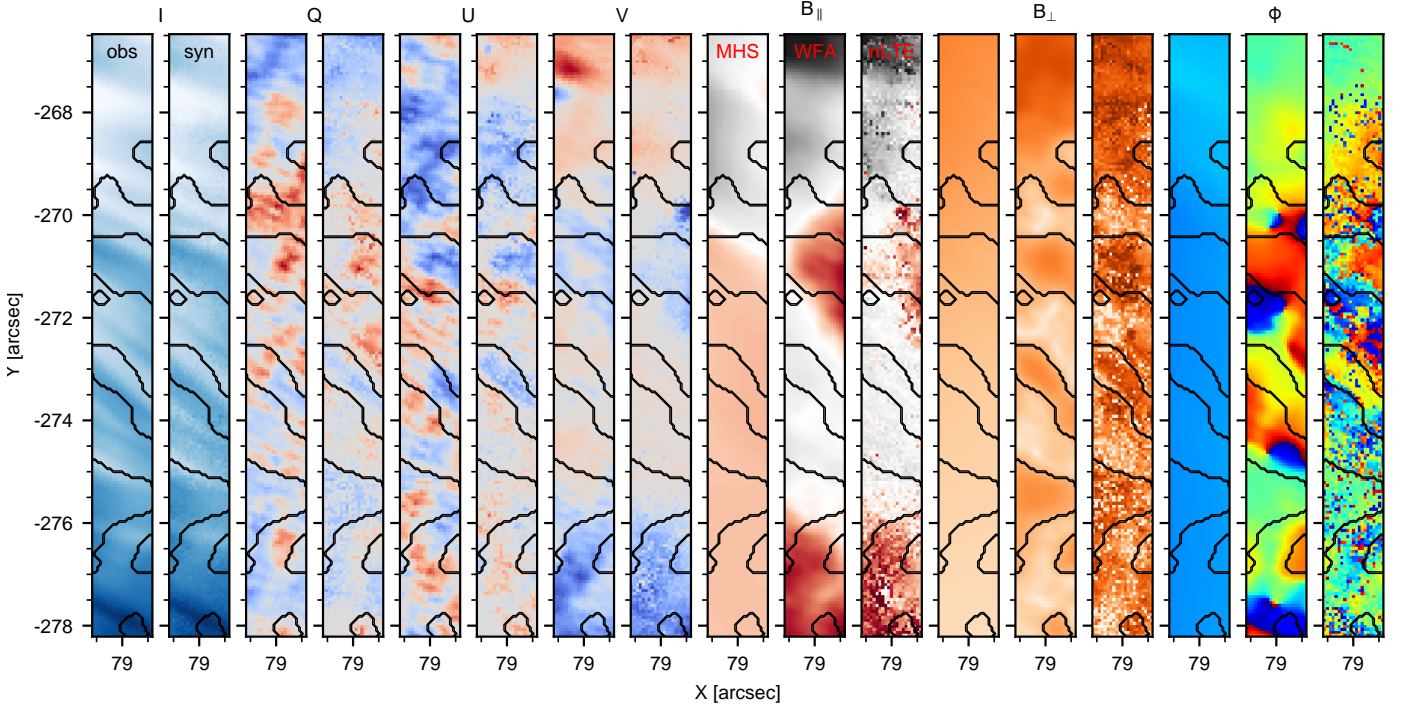


Fig. A.3. Maps of Stokes intensity and magnetic field components for ROI 4. Format as for Fig. A.1.

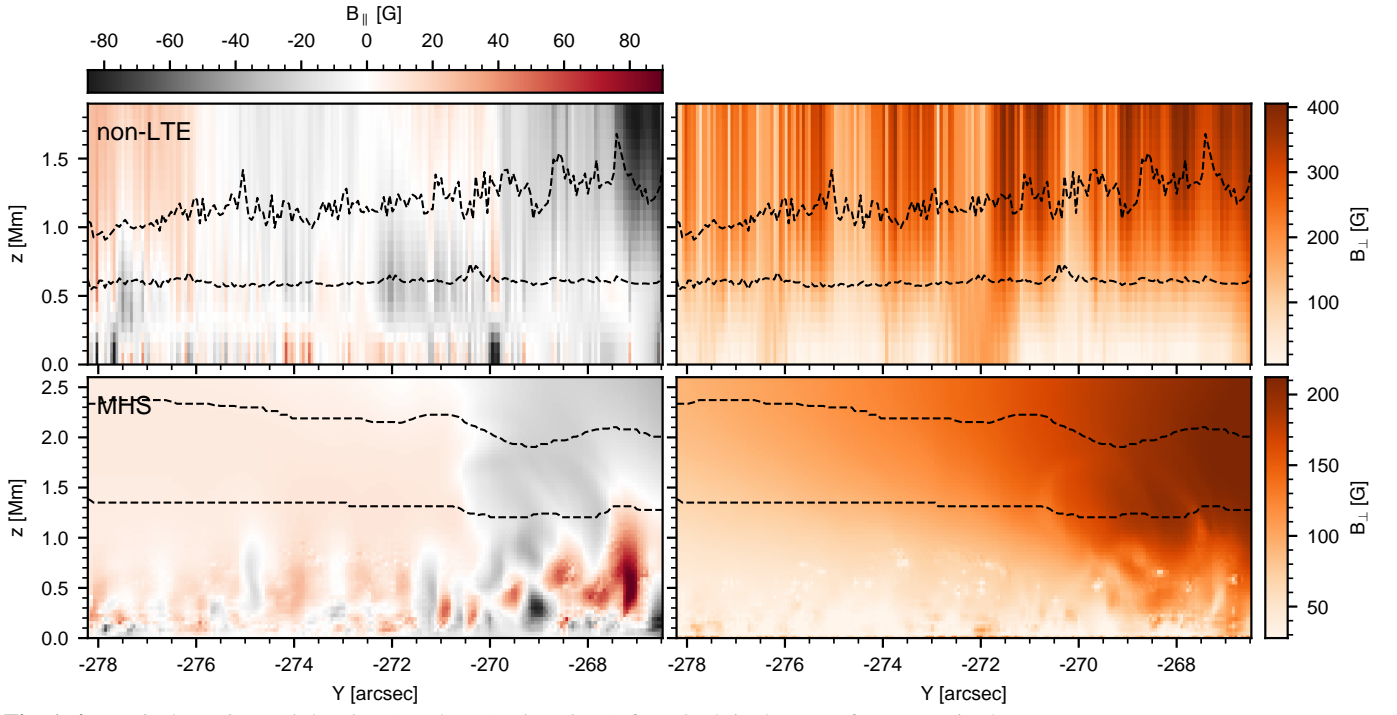


Fig. A.4. Vertical cuts in B_{\parallel} (left column) and B_{\perp} (right column) for ROI 4, in the same format as Fig. 8.